

Optimal limits of cavity optomechanical cooling in the strong coupling regime

Yong-Chun Liu^{1,2}, Yu-Feng Shen¹, Qihuang Gong^{1,2}, and Yun-Feng Xiao^{1,2*}

¹*State Key Laboratory for Mesoscopic Physics and School of Physics,
Peking University, Beijing 100871, P. R. China and*

²*Collaborative Innovation Center of Quantum Matter, Beijing 100871, People's Republic of China*

(Dated: June 18, 2021)

Laser cooling of mesoscopic mechanical resonators is of great interest for both fundamental studies and practical applications. We provide a general framework to describe the cavity-assisted backaction cooling in the strong coupling regime. By studying the cooling dynamics, we find that the temporal evolution of mean phonon number oscillates as a function of the optomechanical coupling strength depending on frequency mixing. The further analytical result reveals that the optimal cooling limit is obtained when the system eigenmodes satisfy the frequency matching condition. The reduced instantaneous-state cooling limits with dynamic dissipative cooling approach are also presented. Our study provides a guideline for optimizing the backaction cooling of mesoscopic mechanical resonators in the strong coupling regime.

PACS numbers: 42.50.Wk, 07.10.Cm, 42.50.Lc

I. INTRODUCTION

Cavity optomechanics [1], which explores the interaction between light and mechanical motion, provides a unique platform for various applications, such as the fundamental test of quantum theory [2], quantum information processing [3] and high-precision measurements [4]. Recent theoretical and experimental efforts have demonstrated optomechanically induced transparency [5], optomechanical storage [6], normal mode splitting [7–9], quantum-coherent coupling between optical modes and mechanical modes [10, 11], state transfer at different optical (electromagnetic) wavelengths [12], quantum entanglement [13], squeezing [14] and nonlinear quantum optomechanics [15]. For most applications, it is a prerequisite to cool the mechanical resonators close to the quantum ground state so as to suppress the thermal noise. In the past few years, numerous experiments have demonstrated cooling of mechanical resonators by employing pure cryogenic cooling [16], feedback cooling (active cooling, or cold-damping) [17] and backaction cooling (passive cooling, or self-cooling) [18–28]. The backaction cooling is proved to be efficient [29–31], especially in the resolved sideband limit, where the mechanical resonance frequency is greater than the decay rate of the optical cavity. Recently many efforts have been taken to extend or improve the backaction cooling, for example, cooling with dissipative coupling [32], cooling with quadratic coupling [33], cooling with hybrid systems [34], cooling in the single photon strong coupling regime [35] and pulsed laser cooling [36].

Besides ground state cooling, another crucial condition for quantum operation is strong coupling [10, 11], where the light-enhanced optomechanical coupling strength ex-

ceeds the cavity decay rate. In such a regime, the optical and mechanical modes hybridize, leading to normal mode splitting [7–9]. In the time domain, the energy exchange between the optical and mechanical modes is reversible, which allows state swapping. However, it also brings about swap heating, which leads to the saturation of cooling rates. To overcome this problem, we have recently [37] proposed a dynamic dissipative cooling approach, which significantly accelerates the cooling process and reduces the cooling limits. In this paper we extend our previous results and present a detailed exploration of the cooling dynamics and cooling limits in the strong coupling regime. We systematically investigate the cooling dynamics under the rotating-wave approximation (RWA) and without RWA. Rabi-like oscillations and frequency mixing phenomenon in the time evolution of mean phonon number are studied. To obtain the lowest cooling limits, we analytically derive the frequency matching condition and a small cavity decay rate is preferred.

The rest of this paper is organized as follows. In Sec. II we use the linearized quantum Langevin equations and quantum master equation to describe the system. In Sec. III we discuss the simplified model under RWA. In Sec. IV we study the full cooling dynamics without the RWA, where the zero-temperature and finite-temperature cases are considered in succession. In Sec. V we discuss the reduced instantaneous-state cooling limits with dynamic dissipative cooling approach. A summary is presented in Sec. VI.

II. THEORETICAL MODEL

We consider a typical optomechanical system involving an optical mode and a mechanical mode, with a coherent laser driving the optical cavity [Fig. 1(a)]. The system Hamiltonian reads $H = \omega_c a^\dagger a + \omega_m b^\dagger b + g a^\dagger a (b + b^\dagger) + (\Omega e^{-i\omega t} a^\dagger + \Omega^* e^{i\omega t} a)$. Here the

*Electronic address: yfxiao@pku.edu.cn; URL: www.phy.pku.edu.cn/~yfxiao/index.html

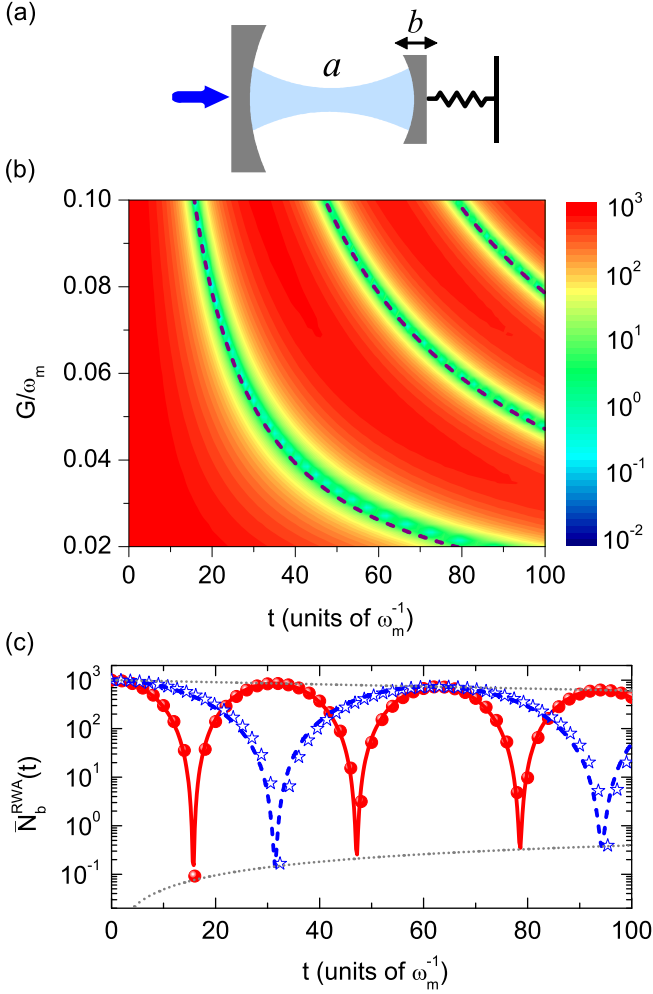


FIG. 1: (color online) (a) Sketch of the optomechanical system. (b) Time evolution of the mean phonon number $\bar{N}_b^{\text{RWA}}(t)$ (under RWA) as functions of t and G for $\Delta' = -\omega_m$, $\kappa/\omega_m = 0.01$, $\gamma/\omega_m = 10^{-5}$ and $n_{\text{th}} = 10^3$. The purple dashed curves correspond to the cases of $t = \pi/(2|G|)$, $3\pi/(2|G|)$ and $5\pi/(2|G|)$. The color bar is in log scale. (c) $\bar{N}_b^{\text{RWA}}(t)$ as a function of t for $G/\omega_m = 0.1$ (red circles and red solid curve) and 0.05 (blue stars and blue dashed curve). The circles and stars are numerical results obtained from Eq. (6) and the curves are analytical results calculated from Eq. (7). The gray dotted curves denote the envelopes given by $n_{\text{th}}e^{-\frac{\kappa+\gamma}{2}t}$ (upper curve) and $n_{\text{th}}(1 - e^{-\frac{\kappa+\gamma}{2}t})\gamma/(\kappa + \gamma)$ (lower curve).

first (second) term describes the energy of the optical (mechanical) mode, with the angular resonance frequency ω_c (ω_m), the annihilation operator a (b) and the creation operator a^\dagger (b^\dagger). The third term represents the optomechanical interaction [38], with the single-photon optomechanical coupling rate g . The last term describes the driving of the input laser, where $\Omega = \sqrt{\kappa_{\text{ex}}}P/(\hbar\omega)e^{i\phi}$ denotes the driving strength with the input laser power P , initial phase ϕ , frequency ω and the input-cavity coupling rate κ_{ex} . In the interaction picture, the quantum

Langevin equations are given by

$$\begin{aligned} \dot{a} &= \left(i\Delta - \frac{\kappa}{2}\right)a - ig a(b + b^\dagger) \\ &\quad - i\Omega - \sqrt{\kappa_{\text{ex}}}a_{\text{in,ex}} - \sqrt{\kappa_0}a_{\text{in},0}, \end{aligned} \quad (1a)$$

$$\dot{b} = \left(-i\omega_m - \frac{\gamma}{2}\right)b - ig a^\dagger a - \sqrt{\gamma}b_{\text{in}}, \quad (1b)$$

where $\Delta = \omega - \omega_c$ denotes the input-cavity detuning; κ_0 stands for the intrinsic cavity dissipation rate; $\kappa = \kappa_0 + \kappa_{\text{ex}}$ represents the total cavity dissipation rate; γ is the dissipation rate of the mechanical mode; $a_{\text{in},0}$, $a_{\text{in,ex}}$ and b_{in} are the noise operators associated with the intrinsic cavity dissipation κ_0 , external cavity dissipation κ_{ex} and mechanical dissipation γ , which have zero mean values and obey the correlation functions $\langle a_{\text{in},0}(t)a_{\text{in},0}^\dagger(t') \rangle = \langle a_{\text{in,ex}}(t)a_{\text{in,ex}}^\dagger(t') \rangle = \delta(t - t')$, $\langle a_{\text{in},0}^\dagger(t)a_{\text{in},0}(t') \rangle = \langle a_{\text{in,ex}}^\dagger(t)a_{\text{in,ex}}(t') \rangle = 0$, $\langle b_{\text{in}}(t)b_{\text{in}}^\dagger(t') \rangle = (n_{\text{th}} + 1)\delta(t - t')$ and $\langle b_{\text{in}}^\dagger(t)b_{\text{in}}(t') \rangle = n_{\text{th}}\delta(t - t')$. Here $n_{\text{th}} = [\exp(\frac{\hbar\omega_m}{k_B T}) - 1]^{-1}$ describes the equilibrium mean thermal phonon number, where T is the temperature of the reservoir and k_B is Boltzmann constant. For strong coherent laser input, both the optical and mechanical modes reach a new steady state, and thus we can rewrite the operators as $a \rightarrow \alpha + a_1$ and $b \rightarrow \beta + b_1$. Here α and β represent the c -number steady state values of the optical and mechanical modes, while a_1 and b_1 are the corresponding fluctuation operators. From Eqs. (1a) and (1b), the quantum Langevin equations for the quantum fluctuations are given by

$$\begin{aligned} \dot{a}_1 &= \left(i\Delta' - \frac{\kappa}{2}\right)a_1 - ig\alpha(b_1 + b_1^\dagger) \\ &\quad - ig a_1(b_1 + b_1^\dagger) - \sqrt{\kappa_{\text{ex}}}a_{\text{in,ex}} - \sqrt{\kappa_0}a_{\text{in},0}, \end{aligned} \quad (2a)$$

$$\begin{aligned} \dot{b}_1 &= \left(-i\omega_m - \frac{\gamma}{2}\right)b_1 - ig(\alpha^* a_1 + \alpha a_1^\dagger) \\ &\quad - ig a_1^\dagger a_1 - \sqrt{\gamma}b_{\text{in}}, \end{aligned} \quad (2b)$$

where $\Delta' = \Delta - g(\beta + \beta^*)$ represents the optomechanical-coupling modified detuning. For strong driving $|\alpha| \gg 1$, the nonlinear terms in Eqs. (2a) and (2b) can be neglected, yielding linearized quantum Langevin equations. The corresponding quadratic Hamiltonian is given by

$$H_L = -\Delta' a_1^\dagger a_1 + \omega_m b_1^\dagger b_1 + (G a_1^\dagger + G^* a_1)(b_1 + b_1^\dagger), \quad (3)$$

where $G = \alpha g$ describes the light-enhanced optomechanical coupling strength. In this Hamiltonian, the rotating-wave terms $G a_1^\dagger b_1 + G^* a_1 b_1^\dagger$ correspond to the beam-splitter interaction, while the counter-rotating-wave terms $G a_1^\dagger b_1^\dagger + G^* a_1 b_1$ describe the two-mode squeezing interaction.

Starting from the Hamiltonian Eq. (3) in the linear regime, the time evolution of the system density matrix

ρ is described by the quantum master equation

$$\begin{aligned} \dot{\rho} = & i[\rho, H_L] + \frac{\kappa}{2} \left(2a_1 \rho a_1^\dagger - a_1^\dagger a_1 \rho - \rho a_1^\dagger a_1 \right) \\ & + \frac{\gamma}{2} (n_{\text{th}} + 1) \left(2b_1 \rho b_1^\dagger - b_1^\dagger b_1 \rho - \rho b_1^\dagger b_1 \right) \\ & + \frac{\gamma}{2} n_{\text{th}} \left(2b_1^\dagger \rho b_1 - b_1 b_1^\dagger \rho - \rho b_1 b_1^\dagger \right). \end{aligned} \quad (4)$$

We focus on the time evolution of the mean phonon number $\bar{N}_b = \langle b_1^\dagger b_1 \rangle = \text{Tr}(\rho b_1^\dagger b_1)$. Using Eq. (4), \bar{N}_b is determined by a linear system of ordinary differential equations involving all the second-order moments $\mathbf{V} = (\bar{N}_a, \bar{N}_b, \langle a_1^\dagger b_1 \rangle, \langle a_1 b_1^\dagger \rangle, \langle a_1 b_1 \rangle, \langle a_1^\dagger b_1^\dagger \rangle, \langle a_1^2 \rangle, \langle a_1^{\dagger 2} \rangle, \langle b_1^2 \rangle, \langle b_1^{\dagger 2} \rangle)^T$ [37, 39], with the equations given by

$$\dot{\mathbf{V}} = \mathbf{M}\mathbf{V} + \mathbf{N}, \quad (5)$$

where $\bar{N}_a = \langle a_1^\dagger a_1 \rangle$, and the elements of the matrices \mathbf{M} and \mathbf{N} are presented in the appendix.

III. COOLING DYNAMICS UNDER THE ROTATING-WAVE APPROXIMATION

We focus on the strong coupling regime, where the light-enhanced optomechanical coupling strength $|G|$ is far greater than the cavity decay rate κ . When $|G| \ll \omega_m$ is also satisfied, the rotating-wave approximation can be made, so that we can concisely describe the main characteristic of the cooling dynamics. Under the RWA, the counter-rotating-wave terms $G a_1^\dagger b_1^\dagger + G^* a_1 b_1$ are neglected, and Eq. (5) reduce to

$$\frac{\partial \bar{N}_a}{\partial t} = -i|G|\bar{F} - \kappa\bar{N}_a, \quad (6a)$$

$$\frac{\partial \bar{N}_b}{\partial t} = i|G|\bar{F} - \gamma\bar{N}_b + \gamma n_{\text{th}}, \quad (6b)$$

$$\frac{\partial \bar{F}}{\partial t} = -2i|G|(\bar{N}_a - \bar{N}_b) - [i(\Delta' + \omega_m) + \frac{\kappa + \gamma}{2}] \bar{F}, \quad (6c)$$

where $\bar{F} = (G\langle a_1^\dagger b_1 \rangle - G^*\langle a_1 b_1^\dagger \rangle)/|G|$ represents the coherence between the optical and mechanical modes. We consider the red sideband resonant case with $\Delta' = -\omega_m$, *i. e.*, the cooling process is on resonance. The time evolution of the mean phonon number is given by

$$\bar{N}_b^{\text{RWA}}(t) \simeq n_{\text{th}} \frac{\gamma + e^{-\frac{\kappa+\gamma}{2}t} \left[\kappa \cos^2(|G|t) - \gamma \sin^2(|G|t) \right]}{\kappa + \gamma}. \quad (7)$$

It shows that the phonon number is proportional to the environmental thermal phonon number n_{th} , which reveals that the rotating-wave optomechanical coupling only modifies the effective mechanical dissipation rate.

In Fig. 1(b) we plot the exact numerical results of $\bar{N}_b^{\text{RWA}}(t)$ as functions of t and G for $\kappa/\omega_m = 0.01$, $\gamma/\omega_m = 10^{-5}$ and $n_{\text{th}} = 10^3$, with Fig. 1(c) plots

both numerical and analytical results of $\bar{N}_b^{\text{RWA}}(t)$ for $G/\omega_m = 0.1$ and 0.05 . It shows that the mean phonon number undergoes Rabi-like oscillations with the period of $\pi/|G|$, which implies the energy exchange between the optical mode and the mechanical mode, together with the normal mode splitting with the frequency difference of $2|G|$. The dissipation is characterized by the envelopes, where the upper envelope is approximately described by $n_{\text{th}} e^{-\frac{\kappa+\gamma}{2}t}$, and the lower envelope reads $n_{\text{th}}(1 - e^{-\frac{\kappa+\gamma}{2}t})\gamma/(\kappa + \gamma)$, as shown in Fig. 1(c). From Figs. 1(b) and (c) we find small discrepancy for small $|G|$, which is because the strong coupling condition is weakly satisfied for $|G| \sim \kappa$. Taking the dissipations into account, the normal mode splitting is given by $\sim 2\sqrt{|G|^2 - \kappa^2/16}$, which is slightly smaller than $2|G|$. Thus the oscillation period is slightly larger than $\pi/|G|$, which agrees with Figs. 1(b) and (c).

When the system reaches the steady state, the final phonon number is given by $n_{\text{th}}\gamma/(\kappa + \gamma)$, as inferred from Eq. (7). Nevertheless, the minimum phonon number is obtained near the end of the first half Rabi oscillation cycle, $t \simeq \pi/(2G)$, with the instantaneous-state cooling limit

$$n_{\text{ins}}^{\text{RWA}} \simeq \frac{\pi\gamma n_{\text{th}}}{4|G|}. \quad (8)$$

It shows that the instantaneous-state cooling limit does not depend on the cavity decay rate κ . This is a great improvement compared with the steady-state cooling limit, which is constrained by the cavity decay rate. In Fig. 2 we plot $n_{\text{ins}}^{\text{RWA}}$ as a function of G . It reveals that a large coupling strength leads to a low cooling limit. This is because the time to reach the minimum is in inverse proportional to the coupling strength, and short evolution time suffers less dissipation, as compared in Fig. 1(c) for $G/\omega_m = 0.1$ and 0.05 . The comparison between the steady-state cooling limit and the instantaneous-state cooling limit is also shown in Fig. 2, which reveals the advantage of the instantaneous-state cooling limit with a factor of $\sim \pi\kappa/(4|G|)$.

IV. COOLING DYNAMICS WITHOUT THE ROTATING-WAVE APPROXIMATION

When the coupling strength $|G|$ is comparable to the mechanical resonance frequency ω_m , the effect of the counter-rotating interactions become important. In this case we need to solve Eq. (5), without the the RWA. For convenience, we first consider the zero-temperature case, where the environmental thermal phonon number n_{th} is set to be zero.

A. Zero-temperature case

For $n_{\text{th}} = 0$, all the initial values of the second-order moments in Eq. (5) are zero. With the time evolution,

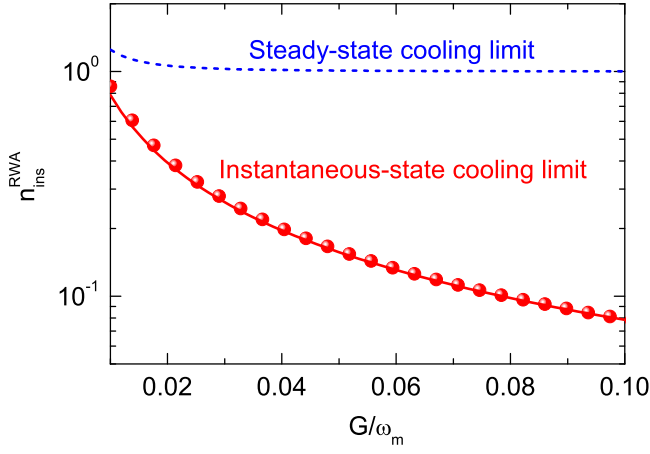


FIG. 2: (color online) Instantaneous-state cooling limit $n_{\text{ins}}^{\text{RWA}}$ as a function of G . The red circles are numerical results obtained from Eq. (6) and the red solid curve is the analytical result calculated from Eq. (8). The steady-state cooling limit is plotted for comparison (blue dashed curve). Other parameters are the same as Fig. 1(b).

these moments become nonzero due to the the quantum backaction resulting from the vacuum fluctuations, i. e., they are created from vacuum by the counter-rotating interactions. For the red sideband resonant case $\Delta' = -\omega_m$, by diagonalizing the Hamiltonian Eq. (3), we obtain $H_L = \omega_+ c_+^\dagger c_+ + \omega_- c_-^\dagger c_-$, where c_\pm are the eigenmodes with the corresponding eigenfrequencies $\omega_\pm = \sqrt{\omega_m^2 \pm 2|G|\omega_m}$. Note that the the eigenfrequencies reduce to $\omega_\pm = \omega_m \pm |G|$ with the RWA as shown in the previous section. The rotating-wave interaction is characterized by the frequency $\omega_+ - \omega_- [\sim 2|G|$ with RWA as appeared in Eq. (7)], while the counter-rotating-wave interaction is characterized by the frequency $\omega_+ + \omega_-$. Therefore, by taking both interactions into consideration, the system dynamics is described by two frequencies $\omega_+ \pm \omega_-$. To provide quantitative results, we derive the time evolution of the mean phonon number in this case as [37]

$$\bar{N}_b^{(0)}(t) \simeq \frac{|G|^2 \left[1 - e^{-\frac{\kappa+\gamma}{2}t} \cos(\omega_+ + \omega_-)t \cos(\omega_+ - \omega_-)t \right]}{2(\omega_m^2 - 4|G|^2)}. \quad (9)$$

Unlike $\bar{N}_b^{\text{RWA}}(t)$ as shown in Eq. (7), here $\bar{N}_b^{(0)}(t)$ does not depend on the environmental thermal phonon number n_{th} , which reveals that it originates from the quantum backaction associated with the vacuum fluctuations.

In Fig. 3(a) we present the exact numerical results of $\bar{N}_b^{(0)}(t)$ as functions of t and G with contour plots. We note that a number of islands regularly appear in the contour map. This is a result of the carrier-envelope-type frequency mixing as described by the term $\cos(\omega_+ + \omega_-)t \cos(\omega_+ - \omega_-)t$ in Eq. (9), where the carrier frequency $\omega_+ + \omega_-$ corresponds to the counter-rotating-wave interaction and the envelope frequency

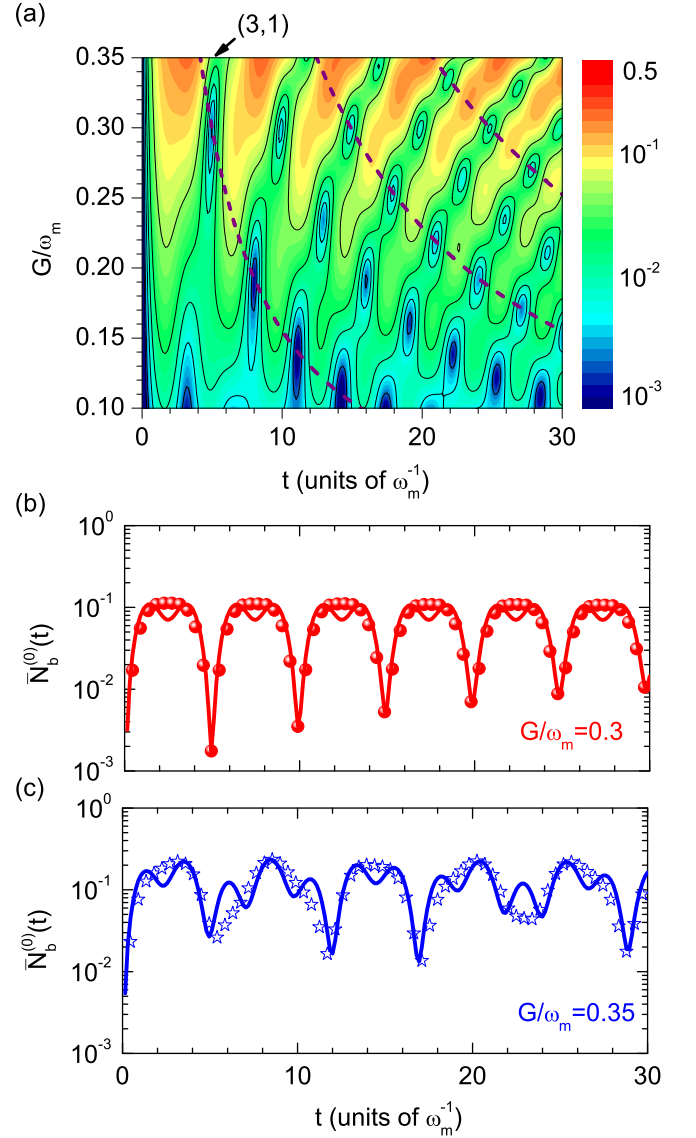


FIG. 3: (color online) (a) Time evolution of the mean phonon number $\bar{N}_b^{(0)}(t)$ as functions of t and G . The purple dashed curves correspond to the cases of $t = \pi/(\omega_+ - \omega_-)$, $3\pi/(\omega_+ - \omega_-)$ and $5\pi/(\omega_+ - \omega_-)$. The island in the top left corner is labeled as $(p, q) = (3, 1)$. The color bar is in log scale. The black contour curves denote $\bar{N}_b^{(0)}(t) = 0.001, 0.002, 0.005, 0.1, 0.2$ and 0.5 . (b) and (c): $\bar{N}_b^{(0)}(t)$ as a function of t for $G/\omega_m = 0.3$ (b) and 0.35 (c). The circles and stars are numerical results obtained from Eq. (5), and the curves are analytical results calculated from Eq. (9). Other parameters are the same as Fig. 1(a) except that $n_{\text{th}} = 0$.

$\omega_+ - \omega_-$ corresponds to the rotating-wave interaction. The local minimum value of $\bar{N}_b^{(0)}(t)$ is obtained when $\cos(\omega_+ + \omega_-)t \cos(\omega_+ - \omega_-)t \simeq 1$, which yields the following frequency matching condition

$$(\omega_+ + \omega_-)t = p\pi, \quad (10a)$$

$$(\omega_+ - \omega_-)t = q\pi, \quad (10b)$$

where p and q are both odd integers or both even integers, and $p > q$. For example, $q = 1, p = 3, 5, 7, \dots$; $q = 2, p = 4, 6, 8, \dots$. We can label these islands in Fig. 3(a) as (p, q) , where we have marked $(3, 1)$ as an example. From Eq. (10) we derive the corresponding $|G|$ and t for each islands (p, q) as

$$|G| = \frac{pq}{p^2 + q^2} \omega_m, \quad (11a)$$

$$t = \sqrt{p^2 + q^2} \frac{\pi}{2\omega_m}. \quad (11b)$$

Because of the dissipation, the optimal minimum value is reached for the island with the shortest time, which corresponds to $(p, q) = (3, 1)$, the labeled island in the top left corner of Fig. 3(a). In this case we obtain $|G|/\omega_m = 0.3$ and $t = \sqrt{10}\pi/(2\omega_m)$. Some of the other minimum values for $q = 1$ [along the leftmost purple dashed curve in Fig. 3(a)] can be obtained as $|G|/\omega_m = p/(p^2 + 1) = 0.19, 0.14, 0.11, \dots (p = 5, 7, 9, \dots)$

In Figs. 3(b) and (c) we plot $\bar{N}_b^{(0)}(t)$ for $G/\omega_m = 0.3$ and 0.35 , corresponding to the frequency matched and unmatched regions, respectively. For the former, the time evolution of phonon number exhibits periodic oscillations, with the minimum phonon number lower than 10^{-3} ; for the latter, the phonon number does not show obvious periodicity, and the minimum phonon number is larger than 10^{-2} . Although there exist some discrepancies between the analytical results expressed by Eq. (9) and the exact results numerically computed from Eq. (5) in the form of some high frequency fluctuations, the analytical expression characterizes the minimum phonon number very well, especially for the frequency-matched case.

For the islands with $q = 1$, the minimum phonon number is obtained near the end of the first half Rabi oscillation cycle, $t \simeq \pi/(\omega_+ - \omega_-)$. The instantaneous-state cooling limit in this case is analytically given by

$$n_{\text{ins}}^{(0)} \simeq \frac{\pi\kappa|G|}{8(\omega_m^2 - 4|G|^2)}, \quad (12)$$

where we have neglected the terms containing mechanical dissipation rate γ since in the experiments typically $\kappa \gg \gamma$. We plot $n_{\text{ins}}^{(0)}$ as a function of G in Fig. 4. The overall trend is that large coupling strength leads to large cooling limit, which is a result of quantum backaction heating in the strong coupling regime. The analytical expression Eq. (12) describes this trend quite well. Meanwhile, the oscillations are signatures of frequency matching, where $|G|/\omega_m = 0.3, 0.19$ and 0.14 correspond to the frequency-matched regions with low phonon number. The steady-state cooling limit reads $|G|^2/[2(\omega_m^2 - 4|G|^2)]$, which is also plotted in Fig. 4 for comparison.

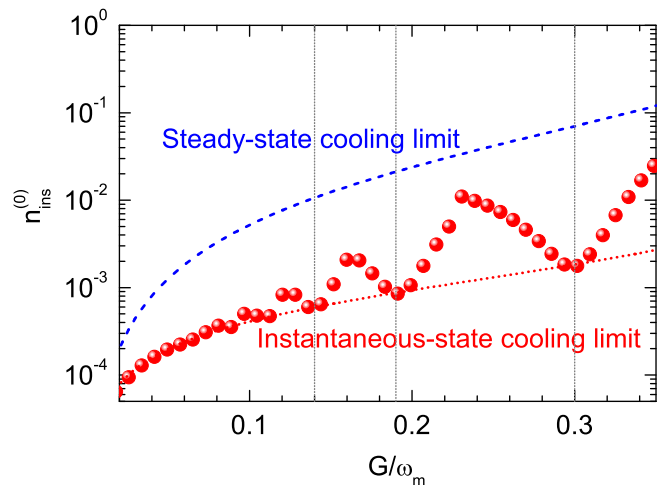


FIG. 4: (color online) Instantaneous-state cooling limit $n_{\text{ins}}^{(0)}$ as a function of G . The red circles are numerical results obtained from Eq. (5) and the red dotted curve is the analytical result calculated from Eq. (12). The steady-state cooling limit is plotted for comparison (blue dashed curve). The dotted vertical lines indicate $G/\omega_m = 0.14, 0.19$ and 0.3 from left to right. Other parameters are the same as Fig. 3(a).

B. Finite-temperature case

For finite-temperature case $n_{\text{th}} \neq 0$, the phonon number originates from both the modified mechanical dissipation and quantum backaction. By solving Eq. (5), in Fig. 5(a) we plot the exact numerical results of the time evolution of the mean phonon number $\bar{N}_b(t)$ as functions of t and G . The contour map shows that $\bar{N}_b(t)$ also exhibits Rabi-like oscillations and a number of islands. The main features of the Rabi-like oscillation is similar to the RWA case as shown in Fig. 1, while the island appears only when both p and q are odd integers, corresponding to the Rabi-like oscillation dips. This is because the contribution of $\bar{N}_b^{(0)}(t)$ is hidden by $\bar{N}_b^{\text{RWA}}(t)$ except for the regions where $\bar{N}_b^{\text{RWA}}(t)$ reaches the minimum, i. e., $\cos(\omega_+ - \omega_-)t \sim -1$, corresponding to odd q . In Fig. 5(b) we compare $\bar{N}_b(t)$ and $\bar{N}_b^{\text{RWA}}(t)$ for both $G/\omega_m = 0.3$ and 0.35 , which demonstrates the significance of frequency matching. For $G/\omega_m = 0.3$ (frequency-matched case), the difference between $\bar{N}_b(t)$ and $\bar{N}_b^{\text{RWA}}(t)$ is small and the minimum phonon number is less than 10^{-1} . However, for $G/\omega_m = 0.35$ (frequency-unmatched case), $\bar{N}_b(t)$ is different from $\bar{N}_b^{\text{RWA}}(t)$ near the Rabi-oscillation dips, since the frequency matching condition is not satisfied. In this case the quantum backaction plays an important role and the minimum phonon number is as large as 10^2 . In Fig. 6(a), we present the instantaneous-state cooling limit n_{ins} [obtained near $t = \pi/(\omega_+ - \omega_-)$] as a function of G (blue stars), which reveals obvious difference between the frequency matched and unmatched cases.

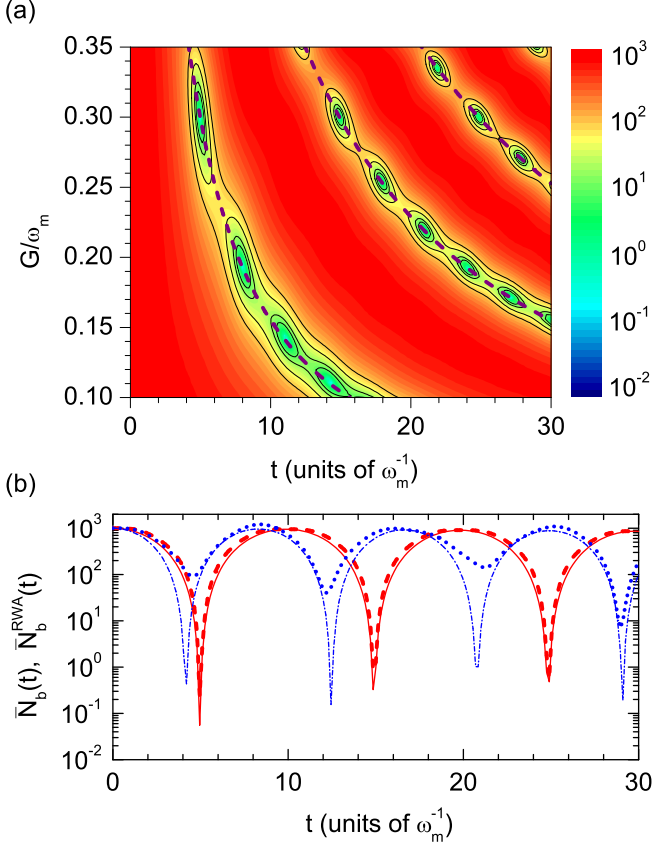


FIG. 5: (color online) (a) Time evolution of the mean phonon number $\bar{N}_b(t)$ as functions of t and G . The purple dashed curves correspond to the cases of $t = \pi/(\omega_+ - \omega_-)$, $3\pi/(\omega_+ - \omega_-)$ and $5\pi/(\omega_+ - \omega_-)$. The color bar is in log scale. The black contour curves denote $\bar{N}_b(t) = 10, 20, 50$ and 100 . (b) $\bar{N}_b(t)$ as a function of t for $G/\omega_m = 0.3$ (red dashed curve) and 0.35 (blue dotted curve), which are numerical results obtained from Eq. (5); $\bar{N}_b^{\text{RWA}}(t)$ as a function of t for $G/\omega_m = 0.3$ (red solid curve) and 0.35 (blue dash-dotted curve), which are numerical results obtained from Eq. (6). Other parameters are the same as Fig. 1(a).

V. REDUCED INSTANTANEOUS-STATE COOLING LIMITS

By employing the dynamic dissipative cooling approach [37], the instantaneous-state cooling limit can be significantly reduced. In Fig. 6(a) we plot the reduced instantaneous-state cooling limits with dynamic cavity dissipation modulation as a function of G for $\kappa/\omega_m = 0.01$ (red circles). Analytical derivations lead to the cooling limits [37]

$$n_{\text{ins}} \simeq \frac{\pi\gamma n_{\text{th}}}{4|G|} + \frac{\pi^2 |G|^4}{(\omega_m^2 - |G|^2)(\omega_m^2 - 4|G|^2)}, \quad (13a)$$

$$n_{\text{ins}}^{\text{opt}} \simeq \frac{\pi\gamma n_{\text{th}}}{4|G|} + \frac{\pi\kappa|G|}{8(\omega_m^2 - 4|G|^2)}, \quad (13b)$$

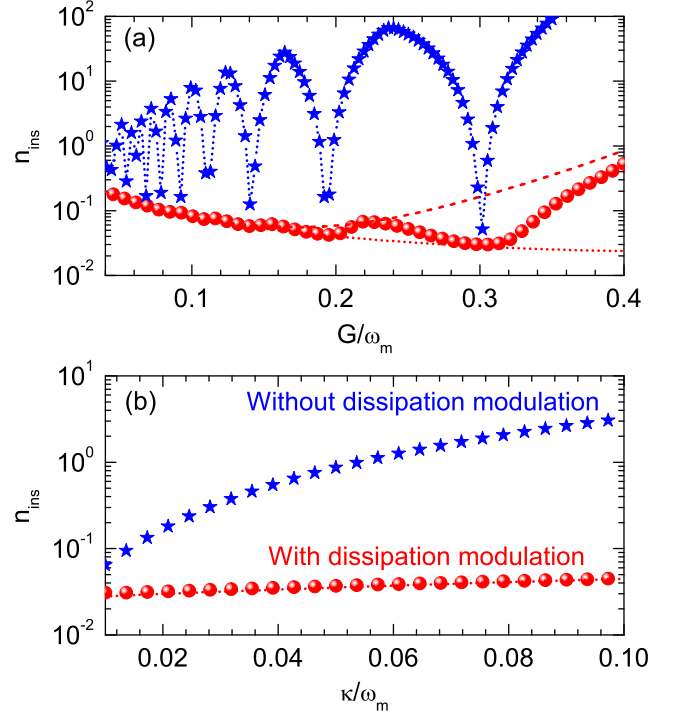


FIG. 6: (color online) (a) Instantaneous-state cooling limits n_{ins} as a function of G for $\kappa/\omega_m = 0.01$. (b) n_{ins} as a function of κ for $G/\omega_m = 0.3$. The red circles are numerical results obtained from Eq. (5) with dynamic cavity dissipation modulation; the red dashed and dotted curves are the analytical results calculated from Eqs. (13a) and (13b); the blue stars are the numerical results obtained from Eq. (5) without dynamic cavity dissipation modulation. Other parameters are the same as Fig. 1(a).

where $n_{\text{ins}}^{\text{opt}}$ denotes the instantaneous-state cooling limits for the optimal coupling strength G (frequency-matched case), and n_{ins} corresponds to the frequency-unmatched case. It reveals that these two expressions set the upper and lower bounds of the instantaneous-state cooling limits, as shown in Fig. 6(a). It is worth noting that the lower bound is the sum of the two cooling limits given by Eq. (8) and Eq. (12), i. e., $n_{\text{ins}}^{\text{opt}} = n_{\text{ins}}^{\text{RWA}} + n_{\text{ins}}^{(0)}$. Typically, the minimum cooling limit is obtained for $|G|/\omega_m = 0.3$, as shown in Fig. 6(a). In Fig. 6(b) the instantaneous-state cooling limits as functions of the cavity decay rate κ for the optimal coupling strength $|G|/\omega_m = 0.3$ are plotted. It shows that a small κ is preferred to obtain a low cooling limit. Therefore, to attain the best cooling performance in the strong coupling regime, the frequency matching condition should be satisfied and a small cavity decay rate is required. This is in contrast to the steady-state cooling limit which requires an optimal value for κ to balance the quantum limit and cavity bandwidth limitation [7, 39].

VI. CONCLUSIONS

In summary, we have examined the backaction cooling of mesoscopic mechanical resonators in the strong coupling regime. When the rotating-wave approximation is satisfied, the mean phonon number undergoes simple damped Rabi-like oscillations with the Rabi frequency of $2|G|$ and the exponential damping envelope scales as $e^{-\frac{\kappa+\gamma}{2}t}$. At the first half oscillation cycle, the minimum mean phonon number is derived as $\pi\gamma n_{\text{th}}/(4|G|)$. For large coupling strength where the rotating-wave approximation fails, the mean phonon number oscillates as functions of both the evolution time and the coupling strength, which is a result of frequency mixing. Under the frequency matching condition, the optimal coupling strengths are derived as $|G|/\omega_m \simeq 0.3, 0.19, 0.14\dots$. By employing the dynamic dissipative approach [37], the reduced instantaneous-state cooling limits reach the lower bound $\pi\gamma n_{\text{th}}/(4|G|) + \pi\kappa|G|/[8(\omega_m^2 - 4|G|^2)]$. This provides a guideline for achieving the lowest cooling limit, which is reached when the frequency matching condition is satisfied and when the cavity decay rate κ is small. Compared with the steady-state cooling limit, the unique advantage is that it does not require an optimal value for κ , allowing for long-coherence-time quantum operations deeply in the strong coupling regime. The parameter

ranges $\gamma \ll \kappa < G < \omega_m/2$ can be realized in various optomechanical systems, for example, in the microtoroid system studied in Ref. [10], with the parameters $\omega_m/2\pi \sim 78$ MHz, $\kappa/2\pi \sim 7.1$ MHz, $\gamma/2\pi \sim 10$ kHz and $G/2\pi \sim 11.4$ MHz, or in the superconducting aluminium membrane system studied in Ref. [11], with the parameters $\omega_m/2\pi \sim 10.5$ MHz, $\kappa/2\pi \sim 320$ kHz, $\gamma/2\pi \sim 35$ Hz and $G > \kappa$.

Acknowledgments

This work is supported by the 973 program (2013CB328704, 2013CB921904), NSFC (11004003, 11222440, and 11121091), and RFDPH (20120001110068). Y.C.L is supported by the Scholarship Award for Excellent Doctoral Students granted by the Ministry of Education. Y.F.S was supported by the National Fund for Fostering Talents of Basic Science (Grants No. J1030310 and No. J1103205)

Appendix A

In Eq. (5), the matrices \mathbf{M} and \mathbf{N} are given by

$$\mathbf{M} = \begin{pmatrix} -\kappa & 0 & -iG & iG^* & iG^* \\ 0 & -\gamma & iG & -iG^* & iG^* \\ -iG^* & iG^* & -i(\Delta' + \omega_m) - \frac{\kappa+\gamma}{2} & 0 & 0 \\ iG & -iG & 0 & i(\Delta' + \omega_m) - \frac{\kappa+\gamma}{2} & 0 \\ -iG & -iG & 0 & 0 & i(\Delta' - \omega_m) - \frac{\kappa+\gamma}{2} \\ iG^* & iG^* & 0 & 0 & 0 \\ 0 & 0 & 0 & -2iG & -2iG \\ 0 & 0 & 2iG^* & 0 & 0 \\ 0 & 0 & -2iG & 0 & -2iG^* \\ 0 & 0 & 0 & 2iG^* & 0 \\ -iG & 0 & 0 & 0 & 0 \\ -iG & 0 & 0 & 0 & 0 \\ 0 & 0 & -iG & iG^* & 0 \\ 0 & iG^* & 0 & 0 & -iG \\ 0 & -iG^* & 0 & -iG & 0 \\ -i(\Delta' - \omega_m) - \frac{\kappa+\gamma}{2} & 0 & iG & 0 & iG^* \\ 0 & 2i\Delta' - \kappa & 0 & 0 & 0 \\ 2iG^* & 0 & -2i\Delta' - \kappa & 0 & 0 \\ 0 & 0 & 0 & -2i\omega_m - \gamma & 0 \\ 2iG & 0 & 0 & 0 & 2i\omega_m - \gamma \end{pmatrix}, \quad (\text{A1})$$

$$\mathbf{N} = (0, \gamma n_{\text{th}}, 0, 0, -iG, iG^*, 0, 0, 0, 0)^T. \quad (\text{A2})$$

Initially, the mean phonon number is equal to the bath thermal phonon number and other second-order moments

are zero, i. e., $\mathbf{V}(t=0) = (0, n_{\text{th}}, 0, 0, 0, 0, 0, 0, 0, 0)^T$.

-
- [1] T. J. Kippenberg and K. J. Vahala, *Science* **321**, 1172 (2008); F. Marquardt and S. M. Girvin, *Physics* **2**, 40 (2009); M. Aspelmeyer, T. J. Kippenberg, F. Marquardt, arXiv:1303.0733 (2013); Y.-C. Liu, Y.-W. Hu, C. W. Wong and Y.-F. Xiao, *Chin. Phys. B* **22**, 114213 (2013).
- [2] O. Romero-Isart *et al.*, *Phys. Rev. Lett.* **107**, 020405 (2011); Z.-q. Yin, T. Li, X. Zhang, and L. M. Duan, *Phys. Rev. A* **88**, 033614 (2013).
- [3] K. Stannigel *et al.*, *Phys. Rev. Lett.* **109**, 013603 (2012).
- [4] M. D. LaHaye, O. Buu, B. Camarota, K. C. Schwab, *Science* **304**, 74 (2004); G. Anetsberger *et al.*, *Nature Phys.* **5**, 909 (2009); J. D. Teufel, R. Donner, M. A. Castellanos-Beltran, J. W. Harlow, and K. W. Lehnert, *Nature Nanotech.* **4**, 820 (2009); A. G. Krause, M. Winger, T. D. Blasius, Q. Lin, O. Painter, *Nature Photon.* **6**, 768 (2012); T. P. Purdy, R. W. Peterson, and C. A. Regal, *Science* **339**, 801 (2013);
- [5] G. S. Agarwal and S. Huang, *Phys. Rev. A* **81**, 041803(R) (2010); S. Weis *et al.*, *Science* **330**, 1520 (2010); A. H. Safavi-Naeini *et al.*, *Nature (London)* **472**, 69 (2011); M. Karuza *et al.*, *Phys. Rev. A* **88**, 013804 (2013).
- [6] V. Fiore *et al.*, *Phys. Rev. Lett.* **107**, 133601 (2011).
- [7] J. M. Dobrindt, I. Wilson-Rae, and T. J. Kippenberg, *Phys. Rev. Lett.* **101**, 263602 (2008).
- [8] S. Gröblacher, K. Hammerer, M. R. Vanner, and M. Aspelmeyer, *Nature (London)* **460**, 724 (2009).
- [9] J. D. Teufel *et al.*, *Nature (London)* **471**, 204 (2011).
- [10] E. Verhagen, S. Deléglise, S. Weis, A. Schliesser, and T. J. Kippenberg, *Nature (London)* **482**, 63 (2012).
- [11] T. A. Palomaki, J. W. Harlow, J. D. Teufel, R. W. Simmonds, and K. W. Lehnert, *Nature (London)* **495**, 210 (2013).
- [12] Y.-D. Wang and A. A. Clerk, *Phys. Rev. Lett.* **108**, 153603 (2012); L. Tian, *Phys. Rev. Lett.* **108**, 153604 (2012); S. Barzanjeh, M. Abdi, G. J. Milburn, P. Tombesi, and D. Vitali, *Phys. Rev. Lett.* **109**, 130503 (2012); J. T. Hill, A. H. Safavi-Naeini, J. Chan, and O. Painter, *Nature Comm.* **3**, 1196 (2012); C. Dong, V. Fiore, M. C. Kuzyk, and H. Wang, *Science* **338**, 1609 (2012); Y. Liu, M. Davanco, V. Aksyuk, and K. Srinivasan, *Phys. Rev. Lett.* **110**, 223603 (2013).
- [13] D. Vitali *et al.*, *Phys. Rev. Lett.* **98**, 030405 (2007); L. Tian, *Phys. Rev. Lett.* **110**, 233602 (2013); Y.-D. Wang and A. A. Clerk, *Phys. Rev. Lett.* **110**, 253601 (2013); H.-K. Li, X.-X. Ren, Y.-C. Liu, Y.-F. Xiao, *Phys. Rev. A* **88**, 053850 (2013); M. C. Kuzyk, S. J. van Enk, and H. Wang arXiv: 1307.2844 (2013).
- [14] D. W. C. Brooks *et al.*, *Nature (London)* **488**, 476 (2012); A. H. Safavi-Naeini *et al.*, *Nature (London)* **500**, 185 (2013); T. P. Purdy, P.-L. Yu, R. W. Peterson, N. S. Kampel, and C. A. Regal, *Phys. Rev. X* **3**, 031012 (2013).
- [15] P. Rabl, *Phys. Rev. Lett.* **107**, 063601 (2011); A. Nunnenkamp, K. Børkje, and S. M. Girvin, *Phys. Rev. Lett.* **107**, 063602 (2011); M. Ludwig, A. H. Safavi-Naeini, O. Painter, and F. Marquardt, *Phys. Rev. Lett.* **109**, 063601 (2012); M.-A. Lemonde, N. Didier, and A. A. Clerk, *Phys. Rev. Lett.* **111**, 053602 (2013); K. Børkje, A. Nunnenkamp, J. D. Teufel, and S. M. Girvin, *Phys. Rev. Lett.* **111**, 053603 (2013); Y.-C. Liu, Y.-F. Xiao, Y.-L. Chen, X.-C. Yu, and Q. Gong, *Phys. Rev. Lett.* **111**, 083601 (2013); A. Kronwald and F. Marquardt, *Phys. Rev. Lett.* **111**, 133601 (2013).
- [16] A. D. O'Connell *et al.*, *Nature (London)* **464**, 697 (2010).
- [17] S. Mancini, D. Vitali, and P. Tombesi, *Phys. Rev. Lett.* **80**, 688 (1998); P.-F. Cohadon, A. Heidmann, and M. Pinard, *Phys. Rev. Lett.* **83**, 3174 (1999); D. Kleckner and D. Bouwmeester, *Nature* **444**, 75 (2006); T. Corbitt *et al.*, *Phys. Rev. Lett.* **99**, 160801 (2007); M. Poggio, C. L. Degen, H. J. Mamin, and D. Rugar, *Phys. Rev. Lett.* **99**, 17201 (2007).
- [18] S. Gigan *et al.*, *Nature (London)* **444**, 67 (2006).
- [19] O. Arcizet, P.-F. Cohadon, T. Briant, M. Pinard, and A. Heidmann, *Nature (London)* **444**, 71 (2006).
- [20] A. Schliesser, P. Del'Haye, N. Nooshi, K. J. Vahala, and T. J. Kippenberg, *Phys. Rev. Lett.* **97**, 243905 (2006).
- [21] A. Schliesser, R. Rivière, G. Anetsberger, O. Arcizet, and T. J. Kippenberg, *Nature Phys.* **4**, 415 (2008).
- [22] S. Gröblacher *et al.*, *Nature Phys.* **5**, 485 (2009).
- [23] Y.-S. Park and H. Wang, *Nature Phys.* **5**, 489 (2009).
- [24] A. Schliesser, O. Arcizet, R. Rivière, G. Anetsberger, and T. J. Kippenberg, *Nature Phys.* **5**, 509 (2009).
- [25] T. Rocheleau *et al.*, *Nature (London)* **463**, 72 (2010).
- [26] J. D. Teufel *et al.*, *Nature (London)* **475**, 359 (2011).
- [27] J. Chan *et al.*, *Nature (London)* **478**, 89 (2011).
- [28] R. Riviere *et al.*, *Phys. Rev. A* **83**, 063835 (2011).
- [29] I. Wilson-Rae, N. Nooshi, W. Zwerger, and T. J. Kippenberg, *Phys. Rev. Lett.* **99**, 093901 (2007).
- [30] F. Marquardt, J. P. Chen, A. A. Clerk, and S. M. Girvin, *Phys. Rev. Lett.* **99**, 093902 (2007).
- [31] C. Genes, D. Vitali, P. Tombesi, S. Gigan, and M. Aspelmeyer, *Phys. Rev. A* **77**, 033804 (2008).
- [32] F. Elste, S. M. Girvin, and A. A. Clerk, *Phys. Rev. Lett.* **102**, 207209 (2009); M. Li, W. H. P. Pernice, and H. X. Tang, *Phys. Rev. Lett.* **103**, 223901 (2009); A. Xuereb, R. Schnabel, and K. Hammerer, *Phys. Rev. Lett.* **107**, 213604 (2011); T. Weiss and A. Nunnenkamp, *Phys. Rev. A* **88**, 023850 (2013); M.-Y. Yan, H.-K. Li, Y.-C. Liu, W.-L. Jin, and Y.-F. Xiao, *Phys. Rev. A* **88**, 023802 (2013).
- [33] A. Nunnenkamp, K. Børkje, J. G. E. Harris, and S. M. Girvin, *Phys. Rev. A* **82**, 021806(R) (2010).
- [34] C. Genes, H. Ritsch, and D. Vitali, *Phys. Rev. A* **80**, 061803(R) (2009); B. Vogell *et al.*, *Phys. Rev. A* **87**, 023816 (2013).
- [35] A. Nunnenkamp, K. Børkje, and S. M. Girvin, *Phys. Rev. A* **85**, 051803(R) (2012).
- [36] M. R. Vanner *et al.*, *Proc. Natl. Acad. Sci. USA* **108**, 16182 (2011); Y. Li, L.-A. Wu, and Z. D. Wang, *Phys. Rev. A* **83**, 043804 (2011); J.-Q. Liao and C. K. Law, *Phys. Rev. A* **84**, 053838 (2011); X. Wang, S. Vinjanampathy, F. W. Strauch, and K. Jacobs, *Phys. Rev. Lett.* **107**, 177204 (2011); S. Machnes *et al.*, *Phys. Rev. Lett.* **108**, 153601 (2012).
- [37] Y.-C. Liu, Y.-F. Xiao, X. Luan, and C. W. Wong, *Phys. Rev. Lett.* **110**, 153606 (2013).
- [38] C. K. Law, *Phys. Rev. A* **51**, 2537 (1995).
- [39] I. Wilson-Rae, N. Nooshi, J. Dobrindt, T. J. Kippenberg and W. Zwerger, *New J. Phys.* **10**, 095007 (2008).